Earth, Planets and Space

FULL PAPER

Open Access

Morphology of sporadic E layers derived from Fengyun-3C GPS radio occultation measurements

Xiaohua Xu[1,2], Jia Luo[1,3*], Han Wang[1], Haifeng Liu[1] and Tianyang Hu[1]

Abstract

The Global Positioning System (GPS) radio occultation (RO) data provided by the Fengyun-3C (FY-3C) mission during January 2015 to December 2019 are used to detect the existence of sporadic E (Es) layers over the globe, based on which the spatial and temporal distributions of the Es occurrence rates (ORs) are presented and analyzed. The results are compared with the Es morphology obtained using the RO data from the Constellation Observing System for the Meteorology, Ionosphere, and Climate (COSMIC) mission. It is found that the seasonal variation patterns of the spatial distributions of Es ORs derived from the FY-3C RO data, which show clearly the effects of wind shear mechanism and the Earth's magnetic field on the formation of Es layers, are basically consistent with those derived from the COSMIC RO data. While the limited local time distribution of the FY-3C RO-detected Es occurrences makes it impossible to resolve the complete diurnal variations of Es layers. Detailed comparisons of the Es morphologies derived from the two different RO missions reveal that the magnitudes of the Es ORs derived by FY-3C data are slightly smaller than those derived by COSMIC data in the middle and low latitudes, which is due to that the top heights of the 50 Hz RO data of FY-3C mission are generally lower than those of the COSMIC mission. In the polar regions, the distinctly low ratio of the FY-3C RO 50 Hz measurements which reach the height of 90 km reduces the capability of these observations for Es-layer detections.

Keywords: Fengyun-3C, COSMIC, GPS radio occultation, Sporadic E Layer, Occurrence rate

*Correspondence: jialuo@whu.edu.cn
[1] School of Geodesy and Geomatics, Wuhan University, 129 Luoyu Road, Wuhan 430079, China
Full list of author information is available at the end of the article

Graphical Abstract

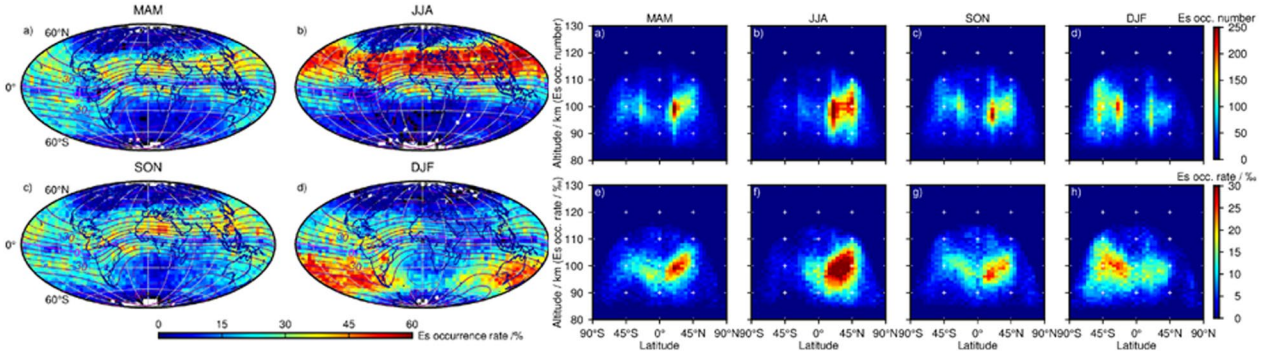

Introduction

Sporadic E (Es) layers, which are also called Es clouds, refer to the irregular-scattered patches of enhanced electron density occurring mainly at the altitude range between 90 and 120 km within the normal E region of the Earth's ionosphere (Arras et al. 2008). Large number of long-lived metallic ions exist in the Es layers, and the mechanism most often employed for the explaining the generation of Es layers is the ion convergence caused by neutral wind shears, which is affected by wind and geomagnetic field (Whitehead 1961; Haldoupis 2012), and other factors such as meteor ionization and thunderstorms also contribute to the formation of Es layers (Whitehead 1970; Mathews 1998). The existence of Es plasma irregularities can cause significant degradation or disturbance of electromagnetic wave propagation, which will cause damage to satellite radio communication and navigation system links (Ogawa et al. 1989).

Measurements from ground-based ionosondes and incoherent scatter radars have been the essential data sources for studying Es plasma irregularities in the past five decades (e.g., Whitehead 1989; Mathews 1998; Haldoupis et al. 2004). With the development of the global navigation satellite system (GNSS) radio occultation (RO) technology, which can provide observations of the atmosphere and ionosphere with global distribution and high vertical resolution, the value of GNSS RO data for the studies of Es layers has been explored and has drawn much attention in recent two decades. During a RO event, the scintillations of the amplitudes and phases of the GNSS signals caused by the Es layers are recorded by the receiver aboard the low earth orbit (LEO) satellite, and can be detected accordingly in different types of RO data products. Since the successful launch of GPS/MET Microlab-1, the first proof-of-concept mission for the GNSS RO technology, data from a series of RO missions, including Microlab-1, the Challenging Minisatellite Payload (CHAMP), the Gravity Recovery and Climate Experiment (GRACE), the Constellation Observing System for the Meteorology, Ionosphere, Climate (COSMIC), etc., have been used to study the irregularities in the lower ionospheric E region (Hocke et al. 2001; Wu et al. 2005; Arras et al. 2008; Zeng and Sokolovskiy 2010; Yeh et al. 2012; Chu et al. 2014; Yue et al. 2015; Arras and Wickert 2018; Xue et al. 2018; Tsai et al. 2018; Chang et al. 2018; Niu et al. 2019; Yu et al. 2019; Qiu et al. 2021). The distributions and variations of RO-observed Es layers have been compared with model simulations or ionosonde/radar measurements, which testified the feasibility and efficiency of using the RO data for Es-related studies. The RO-based Es studies have provided a global overview on Es occurrence and have validated that the mechanisms which modulate the distributions of the Es occurrences and strengths include wind shears, the geomagnetic field, the meteor ionization, and other factors.

The Fengyun-3C (FY-3C) satellite, the first LEO satellite of China which provides GNSS RO observations, was launched in September of 2013 and finally operates in the orbit of 836 km altitude and 98.75° inclination. The National Satellite Meteorological Centre (NSMC) of China is responsible for the data processing of the FY-3C RO data and the publishing of the retrieved atmospheric and ionospheric products. Although the global navigation satellite occultation sounder (GNOS) aboard the FY-3C satellite is able to track the occultation signals of both GPS and BDS simultaneously (Mao et al. 2016), only the GPS RO data and products are provided by the NSMC so far.

The quality of the FY-3C RO ionospheric products have been validated in previous studies. Wang et al. (2019) found that good agreements exist among the ionospheric peak parameters derived by FY-3C RO and

those provided by COSMIC RO and ionosondes over the globe during 2014 to 2017, which supports that the ionospheric products provided by FY-3C RO are reliable enough for further ionospheric and geophysical applications. Bai et al. (2019) verified that the ionospheric F-layer maximum scintillation indexes probed by FY-3C and COSMIC are of high consistency, while till now, work about the application of FY-3C RO data in Es layers-related studies is very seldom. Yang et al. (2016) for the first time attempted to derive the information of Es perturbation from the 50 Hz L1 SNR data of FY-3C GPS RO observations. In their work, the RO data of 4 months, including June, August, December, and January during 2014/2015, were used for studying the variations of the distributions of Es intensity. Diurnal variations of the Es scintillations in different months were concerned about the most by them and the Es-layer scintillations over the middle latitudes of the north hemisphere (NH) during all local time periods are derived, while the GPS RO observations provided by FY-3C mission should not be able to fully resolve the diurnal cycle of Es layers at low- and mid-latitudes due to the near-polar sun-synchronous orbit of the satellite (Pirscher et al. 2007). Although they also presented the latitude–month distribution of Es-layer occurrence rates (ORs) during June 2014 to May 2015, the largest Es ORs in the 10° latitude × 1-month grids are only about 0.06%, which needs further validation. On the other hand, typical features such as the decrease of Es occurrence and intensities in the South Atlantic Anomaly (SAA) zone and the Northern America were not mentioned in their work. In the present study, the long-term global Es morphology is derived based on FY-3C RO observations. The RO data during the time period from January 2015 to December 2019 are used here, which is much longer than that concerned about by Yang et al. (2016). Detailed information about the spatial and temporal distributions of the FY-3C RO-derived Es ORs is presented and analyzed. To validate the FY-3C RO-derived Es morphology, the seasonal variations of the distributions of the FY-3C RO-derived Es-layer ORs are further compared with those derived from the COSMIC RO data during the same time period. Section "Data and methods" describes the original data set from the FY-3C RO mission used in the present study, the method for detecting Es layers, and the general distribution of the FY-3C RO-derived Es layers. Seasonal variations in the spatial and temporal distributions of the FY-3C RO-derived Es ORs are presented in the succeeding section. In Sect. "Discussion", the morphology of Es derived from the FY-3C RO data is further compared with that derived from the COSMIC RO data of the same time period, and the reasons for the inconsistence are analyzed. Conclusions are drawn in the last section.

Data and methods

The "AE" data files of FY-3C RO mission during January 2015 to December 2019, which are provided by the NSMC of China, are used in the present study. Similar to the "atmPhs" file of COSMIC mission provided by the COSMIC Data Analysis and Archive Center (CDAAC) (Yue et al. 2015; Tsai et al. 2018), for each FY-3C RO event, the "AE" file provided by NSMC includes the coordinates of the GPS and LEO satellites in the Earth Center Inertial (ECI) system, phases and SNRs at both L1 and L2 bands, which are all with the sampling rate of 50 Hz. The upper limit of the high-rate occultation data can reach the altitudes between 120 and 125 km, and small-scale fluctuations in the amplitudes of GPS signals caused by the Es layers are detectable in the SNR profiles, which are of high vertical resolution. The SNR profiles at L1 band are used here for the detection of Es layers. For the validation of the Es-layer distributions retrieved from FY-3C RO data, the 50-Hz SNR profiles at L1 band obtained from the COSMIC RO mission during the same time period, which are provided in the "atmPhs" files published by the CDAAC, are also used for detecting Es layers.

The bottom heights of the original 50-Hz SNR profiles of FY-3C RO mission are generally lower than 60 km. For each SNR profile with a top height higher than 80 km, the corresponding truncated profile from around 60 km to the RO observation top is processed. For different RO events, the ranges of the magnitudes of the original GPS L1 SNR sequences vary greatly. So the truncated SNR profiles are at first normalized to get profiles with different background SNR values to the same level. For each truncated SNR profile, the corresponding background SNR profile, SNR_0, is obtained based on the original SNR data as the moving average sequence over a 101-point running window (Liao et al. 2016), which corresponds to the time window of about 2 s and the vertical scale of about 6.0 km, and the normalized SNR profile, SNR_{norm}, is derived as SNR/SNR_0 (Xue et al. 2018). The standard deviations (STDs) of the SNR_{norm} sequence are further calculated over a 51-point running window, which corresponds to the vertical scale of about 3.0 km. In the altitude range of 80 km to 125 km, if the STD value exceeds an empirically threshold of 0.2 and large STD values are concentrated within an altitude range of less than 10 km, then it is considered that the original SNR profile is detected with the signature of sporadic E layer, and the height of the Es layer is determined as the height with the largest STD value (Arras and Wickert 2018). In the subsequent analyses, an Es OR value is calculated as the ratio

of the number of the profiles detected with Es layers to the corresponding total number of truncated SNR profiles processed.

The two subfigures of Fig. 1 present two typical L1 SNR profiles of FY-3C RO events and the corresponding Es-layer detection process. In each of the two subfigures, the identifier of each RO event is shown in the upper right corner of the subfigure, and the original SNR profile, the normalized SNR profile, and the STD profile of the corresponding FY-3C RO event are presented. Following the above procedure, as shown in Fig. 1a and b, the RO event "FY3C_20160101_0516_G18" is detected with no Es layer, while the RO event "FY3C_20160101_0819_G17" is detected with the Es layer at the altitude of around 95.8 km.

For a specific SNR profile, the horizontal position and the height of each SNR data sample are determined using the coordinates of GPS and LEO satellites at the same sampling time, which are also available in the same "AE" data file (FY-3C). And for each sampling, the three-dimensional position of the RO tangent point, which is regarded as the position corresponding to the sampling, is determined from the ECI coordinates of the satellites and is further transferred to the Earth-center, Earth-fixed (ECEF) coordinates, from which the latitude, longitude and the height of the sampling are obtained.

The above Es-layer detection process is carried out on all the L1 SNR profiles extracted from the "AE" files of the FY-3C RO dataset during January 2015 to December 2019. What needs to be mentioned is that some "AE" data files are excluded from the Es detection process due to that the SNR data in these files are invalid values or the top heights of the data sequences are lower than 80 km.

We analyzed 822,320 FY-3C RO measurements in total and among them 142,078 measurements include Es signatures. Figure 2a and b presents the spatial distribution of the number of all available FY-3C RO observations stored in the "AE" files and those observations detected with Es layers, respectively. It can be seen from Fig. 2a that, similar to the spatial distribution of the COSMIC RO observations shown by Chu et al. (2014), there is a significant latitudinal dependence of the number of the original FY-3C RO measurements. Specifically, over the whole globe, the number of the FY-3C RO measurements in a $5^\circ \times 5^\circ$ grid varies from around 0 to around 600, and the largest gridded values of the RO observation numbers are obtained at the middle latitude regions of the two hemispheres. Over each of the two hemispheres, the numbers of the RO measurements in the latitude zones of around 20° and 50° are distinctively larger than those over the tropics and polar regions. Figure 2b presents that Es layers mainly occur in the middle latitudes of the two hemispheres, and more RO observations in the NH are detected with Es layers compared with the SH. During 2015 to 2019, the highest number of the RO observations detected with Es layers in a $5^\circ \times 5^\circ$ grid reaches around 200. Figure 2b also demonstrates distinctly the impact of the geomagnetic field on the distribution of the detected Es layers, which will be depicted in detail in the following analysis about the seasonal variations of Es ORs.

Figure 3 presents the monthly variations of the total number of the FY-3C RO observations, the number of the observations which are valid for Es detections, i.e., the observations with top heights higher than 80 km, the number of the profiles detected with Es layers, and the Es ORs. For each month, the Es OR value is calculated as

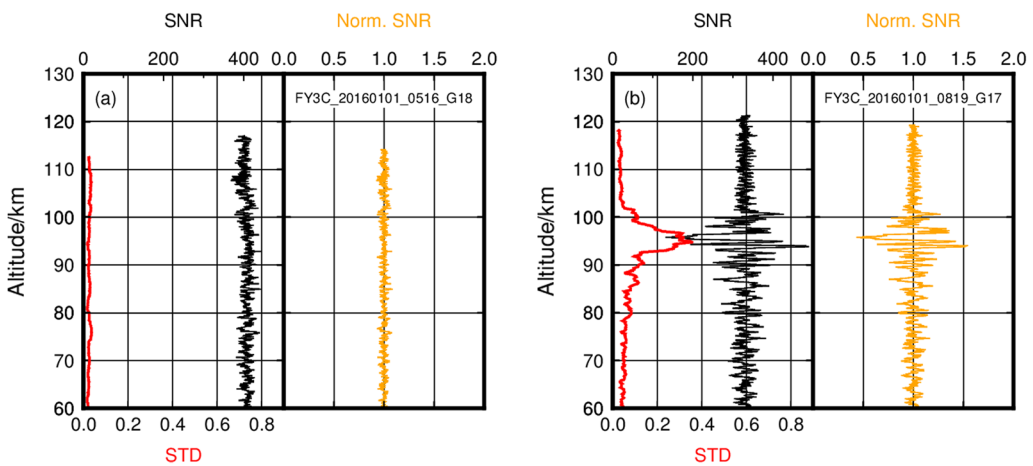

Fig. 1 Examples of the FY-3C RO observations for Es-layer detection for **a** without Es layers, **b** with an Es layer. In each subfigure, the three profiles represent the original L1 SNR profile (in black), the normalized SNR profile (in yellow), and the STD profile (in red), and the identifier of each RO event is shown in the upper right corner of the subfigure

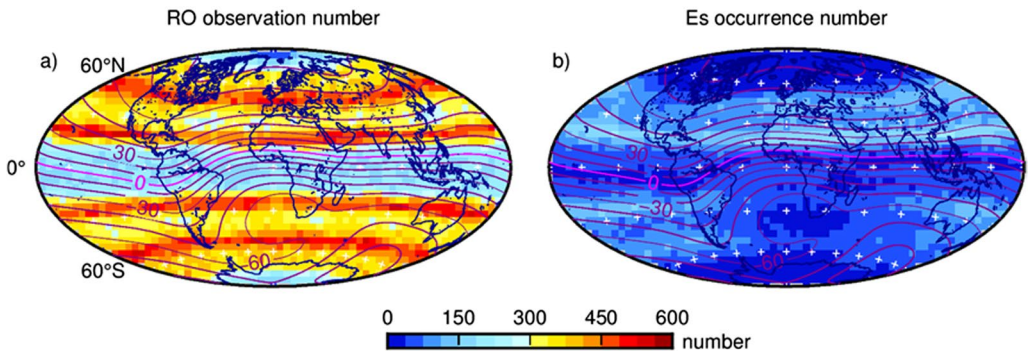

Fig. 2 Spatial distribution of the numbers of **a** all FY-3C RO 50-Hz observations and **b** FY-3C RO observations with Es events, which are binned within a grid of 5° × 5° for the period from January 2015 to December 2019. The pink curve represents the geomagnetic equator and the red curves represent the geomagnetic inclination isolines

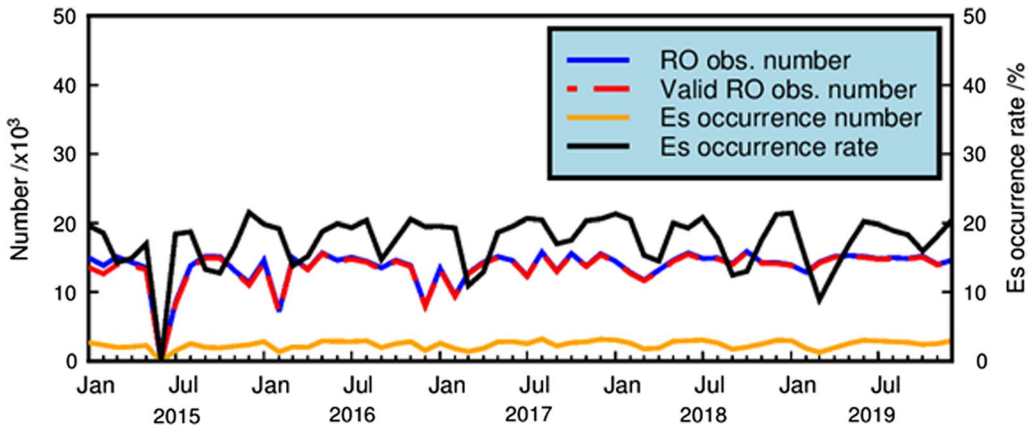

Fig. 3 Monthly variations of the number of all FY-3C RO measurements (in blue), the number of RO measurements valid for Es-layer detection (in red), the number of RO observations detected with Es layers (in yellow), and the Es occurrence rates (in black, right y-axis), during 2015 to 2019

the ratio of the number of the profiles detected with Es layers to the number of valid RO observations. FY-3C RO data during June 1, 2015 to July 12, 2015 are not available at the website of NSMC, which is the reason why on all the four lines shown in Fig. 3, the values corresponding to June 2015 decrease to zero. From Fig. 3, it can be seen that except for June 2015, the monthly numbers of the original FY-3C RO measurements generally vary between 10,000 and 16,000, among which about 98% are valid for Es detections, which leads to the monthly Es ORs varying between 9 and 22%.

Distributions of the FY-3C RO-derived Es occurrence rates

Figure 4 demonstrates the time series of the Es ORs, in which data of 1 month in each 5° latitude band from Jan. 2015 to Dec. 2019 are presented. It can be seen that

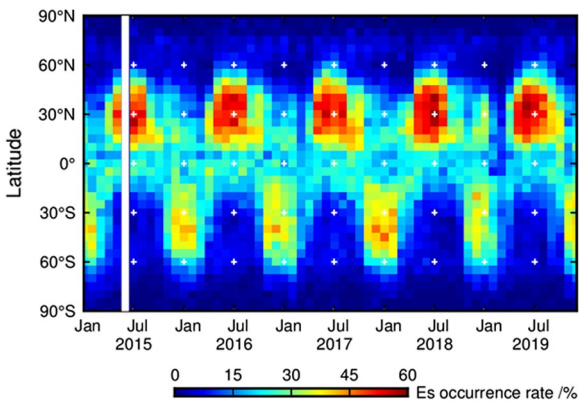

Fig. 4 Time series of the FY-3C RO-derived Es-layer occurrence rates during Jan. 2015 to Dec. 2019, with a resolution of a 5° latitude × 1-month grid Fig. 7 The local time distribution of FY-3C GPS RO events number during Jan 2015 to Dec 2019

the pattern of the latitude–month variation of Es-layer ORs derived using FY-3C RO observations is similar to those derived using CHAMP (Arras et al. 2008) and COSMIC RO observations (Chu et al. 2014), although different time periods are concerned about in these previous studies. Specifically, in each year, Es layers mainly occur during May to September over the latitude band of 20°N–50°N and during November to March over 20°S–50°S. The actual summer maximum (winter minimum) of Es OR can be explained by neutral wind shear effect (Arras et al. 2008; Chu et al. 2014). Moreover, Fig. 4 presents that the Es OR is generally higher in the NH summer than in the SH summer, which is also consistent with Arras et al. (2008) and Qiu et al. (2019).

Figure 5 presents the global distributions of the FY-3C RO-derived Es-layer ORs during four different seasons with the resolution of a $5° \times 5°$ grid. The white grids, each of which is of less than 3 Es events, are not considered. The seasons are categorized here as MAM (March, April, and May), JJA (June, July, and August), SON (September, October, and November) and DJF (December, January, and February). It can be seen from Fig. 5 that in general, the seasonal variation pattern of the horizontal distribution of the FY-3C RO-derived Es ORs is consistent with that obtained by previous studies using the COSMIC RO measurements (Arras et al. 2008; Chu et al. 2014). Specifically, during each season, the Es OR derived from the FY-3C RO observations generally follows the geomagnetic inclination isolines. The peaks of Es-layer ORs occur over the middle latitudes of the summer hemisphere, which are around 60%, while over the winter hemisphere, Es activity is significantly less active. Moderate Es ORs are obtained in the lower latitudes of both hemispheres, which are less than 30%. The Es-layer ORs are larger over the NH than over the SH in general. Besides, the Es-layer ORs decrease over two regions, the South Atlantic Anomaly (SAA) zone and Northern America, which can be figured out in all the four seasons and is shown distinctly in JJA and SON, when the Es occurrence over these two regions are much weaker than anywhere else along the same magnetic latitude bands. This is due to the significant depressions of the horizontal component of Earth's magnetic field in these two areas (Arras et al. 2008; Chu et al. 2014). Another feature which can be figured out from Fig. 5 is that during all the four seasons, the Es activities are extremely low near the magnetic equator, which is due to that the nearly horizontal magnetic field lines over this region prohibit the vertical movement and layered deposition of ionized particles (Arras et al. 2008; Niu et al. 2019). Moreover, the Es ORs are generally lower than 15% in the regions with latitudes higher than 70° over the two hemispheres, which is due to that wind shear mechanism does not work efficiently at polar regions (Haldoupis 2012).

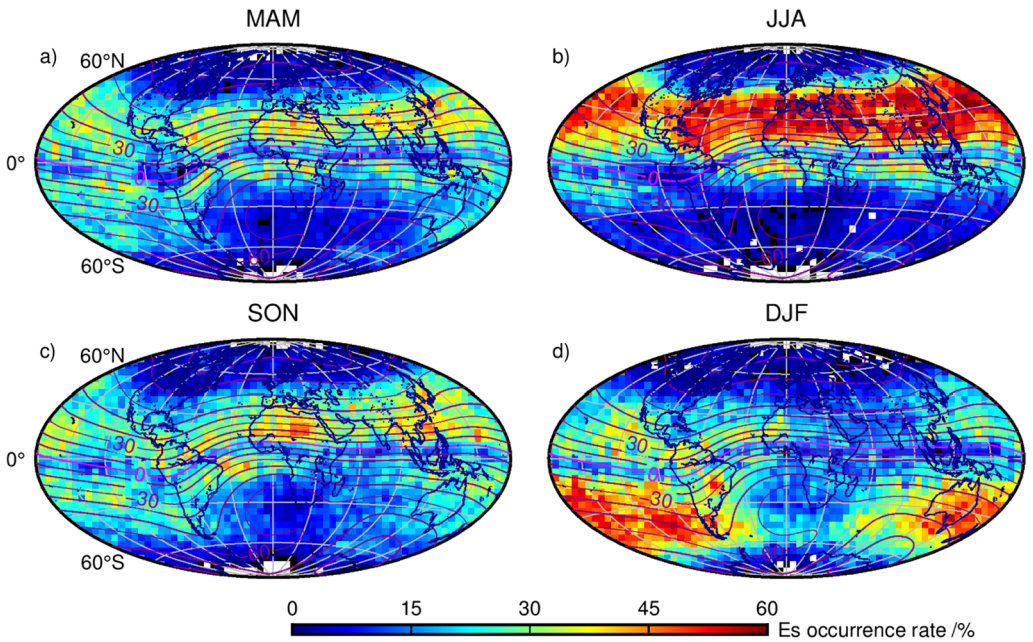

Fig. 5 Seasonal variation in the horizontal distributions of the FY-3C RO-derived Es occurrence rates during Jan. 2015 to Dec. 2019, with the resolution of a $5° \times 5°$ grid. Plots for **a** March, April and May (MAM); **b** Jun, July, and August (JJA); **c** September, October, and November (SON), and **d** December, January, and February (DJF). In each subfigure, the pink curve represents the geomagnetic equator and the red curves represent the geomagnetic inclination isolines

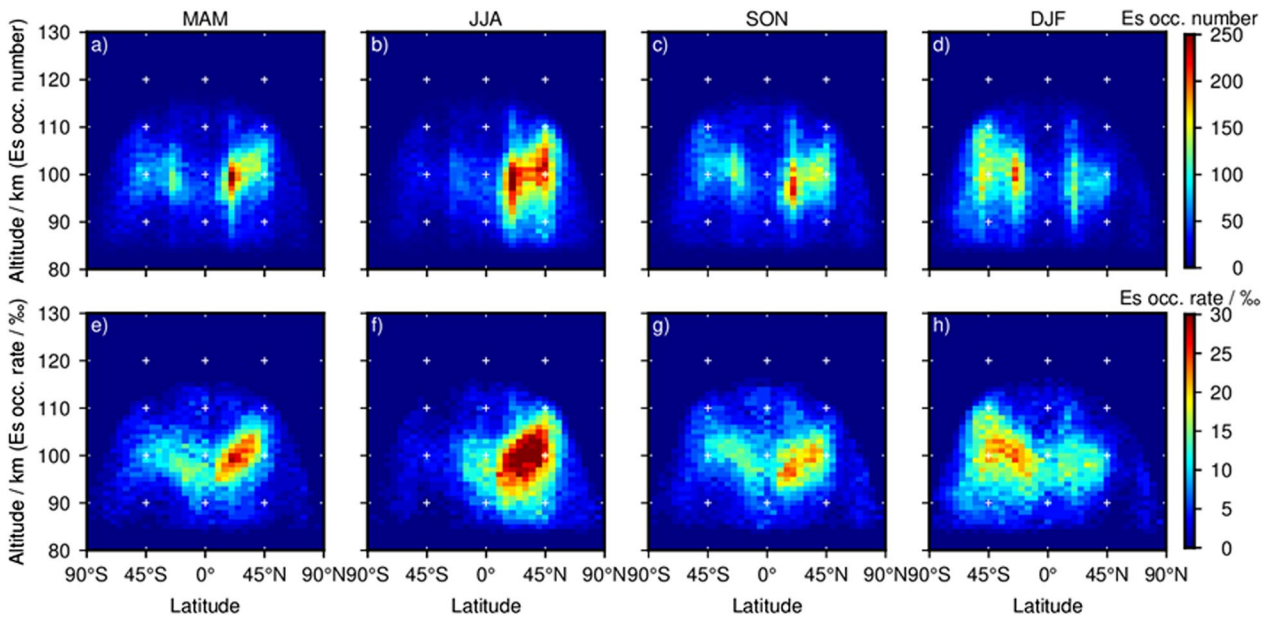

Fig. 6 Seasonal variation in the altitude–latitude distributions of FY-3C RO-derived Es occurrence numbers (upper panels) and Es occurrence rates (lower panels) during Jan. 2015 to Dec. 2019, with a resolution of 1 km × 5° latitude. Plots for four different seasons **a**, **e** MAM; **b**, **f** JJA; **c**, **g** SON and **d**, **h** DJF

Figure 6 presents the seasonal variations of the altitude–latitude distributions of Es occurrence numbers and ORs, with a resolution of 1 km × 5° latitude. For each 1 km × 5° latitude grid, the OR is calculated as the ratio of the Es occurrence number in this grid to the valid FY-3C RO observation number of the corresponding latitude band. It can be seen that the altitude–latitude distribution patterns of both the Es occurrence numbers and Es ORs shown in Fig. 6 are basically consistent with those of the Es ORs shown in Arras et al. (2008) and Chu et al. (2014). Specifically, during all the four seasons, Es layers mainly occur at the altitude range of 90–110 km over the middle latitudes of the two hemispheres, and the heights corresponding to the largest Es occurrences are slightly higher during summer and winter seasons over the summer hemispheres than during equinoxes. The peaks of the ORs are obtained at around 105 km over 25° N to 50° N during the NH summer.

Figure 7 presents the local time (LT) distribution of the original FY-3C GPS RO observations during 2015 to 2019. It can be seen that FY-3C GPS RO events mainly occur during two local time periods, 8:00–12:00 LT and 20:00–24:00 LT. Figure 8 further shows the spatial distributions of the FY-3C GPS RO events in each 1-h local time intervals during these two local time periods. From Fig. 8, it can be seen that due to the near-polar sun-synchronous orbit characteristic of the FY-3C satellite, for a certain 1-h local time interval, the distributions of the RO events over the western hemisphere

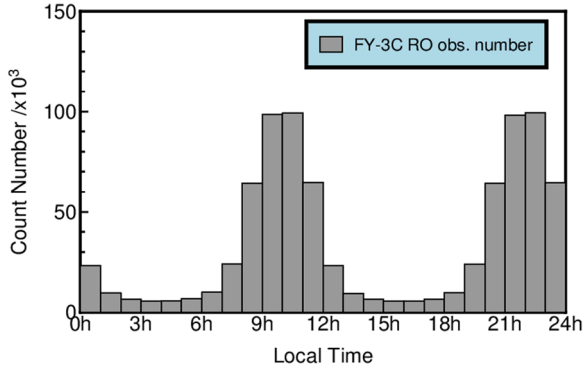

Fig. 7 The local time distribution of FY-3C GPS RO events number during Jan. 2015 to Dec 2019

(WH) and the eastern hemisphere (EH) are not symmetric. Specifically, in the time intervals of 8:00–9:00 LT and 20:00–21:00 LT, most RO observations occur over the EH. While in the time intervals of 11:00–12:00 LT and 23:00–24:00 LT, most FY-3C RO observations occur over the WH. Only in the four 1-h local time intervals of 9:00–10:00 LT, 10:00–11:00 LT, 21:00–22:00 LT, and 22:00–23:00 LT, at all the latitude bands, considerable numbers of RO observations are obtained over both the WH and the EH. So when presenting the latitude–local time distributions of the Es ORs over the globe, only the local time intervals of 9:00–11:00 LT and 21:00–23:00 LT are considered, which is aimed to ensure that the Es ORs for a certain latitude–local time

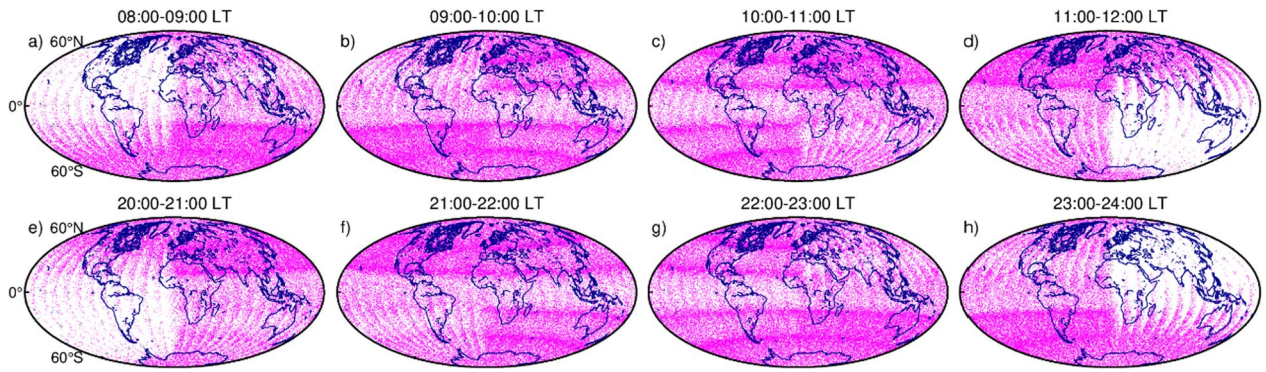

Fig. 8 Spatial distributions of FY-3C GPS RO events for different 1-h local time intervals during Jan. 2015 to Dec. 2019. Plots for local time intervals **a** 8:00–9:00 LT, **b** 9:00–10:00 LT, **c** 10:00–11:00 LT, **d** 11:00–12:00 LT, **e** 20:00–21:00 LT, **f** 21:00–22:00 LT, **g** 22:00–23:00 LT, and **h** 23:00–24:00 LT

grid can to a large extent represent the average ORs over the whole latitude band during the corresponding gridded local time interval.

Figure 9 presents the seasonal variation in the latitude–local time distributions of the Es ORs derived from FY-3C RO observations during the two selected local time periods, 9:00–11:00 LT and 21:00–23:00 LT. It is shown that in the seasons of JJA and DJF, Es layers mainly occur at the middle latitude bands of the summer hemisphere. In the seasons of MAM and SON, during 9:00–11:00 LT, the Es ORs at middle latitudes of the NH are higher than other regions, while the differences between the NH and the SH are not so distinct as the same local time period of JJA and DJF. During 21:00–23:00 LT, the distributions of the Es occurrences are basically symmetric with respect to the equator. Moreover, in all the four seasons, the Es ORs are generally higher during 9:00–11:00 LT than during 21:00–23:00 LT.

It should be noted that when interpreting the day–night differences of the Es ORs shown in Fig. 9 by comparing it with those derived by ionosonde observations, two issues need to be taken into consideration besides that the methods for identifying Es layers from the two types of observations are different. One issue is that day–night difference exists in the spatial distribution of the FY-3C GPS RO events. Although in the local time intervals selected by us, the RO observations cover both the WH and the EH at all the latitudes, the variation of the spatial distribution pattern of FY-3C GPS RO observations during the four different 1-h local time intervals is still distinct. Taking the comparison between 9:00–10:00 LT and 22:00–23:00 LT as an example, the RO events are significantly denser over the Northeast hemisphere (NEH) than over the Northwest hemisphere (NWH) during 9:00–10:00 LT, while during 22:00–23:00 LT, the contrary is the case.

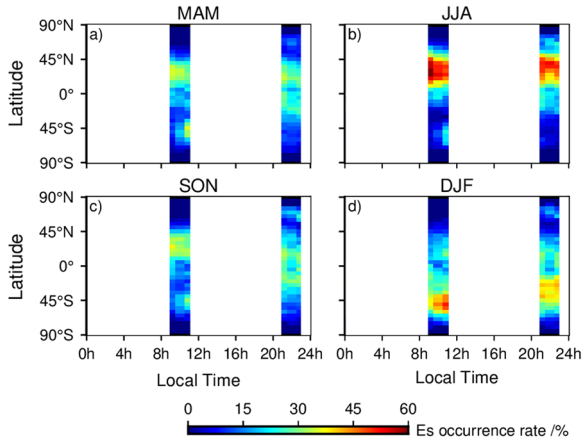

Fig. 9 Seasonal variation in the latitude–local time distributions of FY-3C RO-derived Es occurrence rates for the two local time periods, 9:00–11:00 LT and 21:00–23:00 LT, during Jan. 2015 to Dec. 2019, with a resolution of 5° latitude × 1 h. Plots for four different seasons **a** MAM, **b** JJA, **c** SON, and **d** DJF

Accordingly, the Es ORs of the NH mid-latitudes presented in Fig. 9 should be more affected by the ionosphere condition of the NEH than that of the NWH during 9:00–10:00 LT, while during 22:00–23:00 LT, the contrary is the case. In comparison, the meaning of the local time variation of the Es ORs obtained by ionosonde observations is more explicit, which is derived over the specific location of an ionosonde station. The other issue which needs to be noted is that only the Es layers below the top heights of the 50 Hz FY-3C RO data, which are mostly lower than 120 km, are taken into account in Fig. 9. In comparison, ionosondes can detect the Es layers which occur at altitudes higher than 130 km (Zhou et al. 2017).

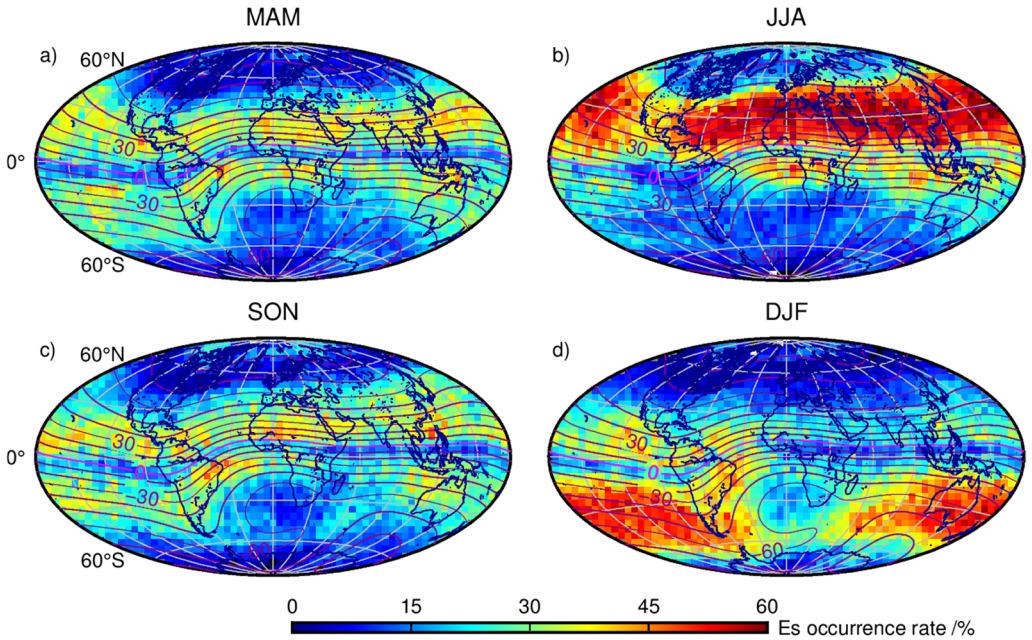

Fig. 10 Seasonal variation in the horizontal distributions of COSMIC RO-derived Es occurrence rates during Jan 2015 to Dec 2019

Discussion

The Es-layer detection algorithm introduced in Sect. 2 is also applied on the 50 Hz L1 SNR data from the COSMIC RO mission during 2015 to 2019. Among all the 1,201,806 COSMIC RO observations, 256,867 measurements are detected with Es signatures. Figure 10 and Fig. 11 present the seasonal variations of the latitude–longitude and the altitude–latitude distributions of the COSMIC RO-derived Es ORs. The comparison between Fig. 10 and Fig. 5 and that between Fig. 11 and Fig. 6 shows that the

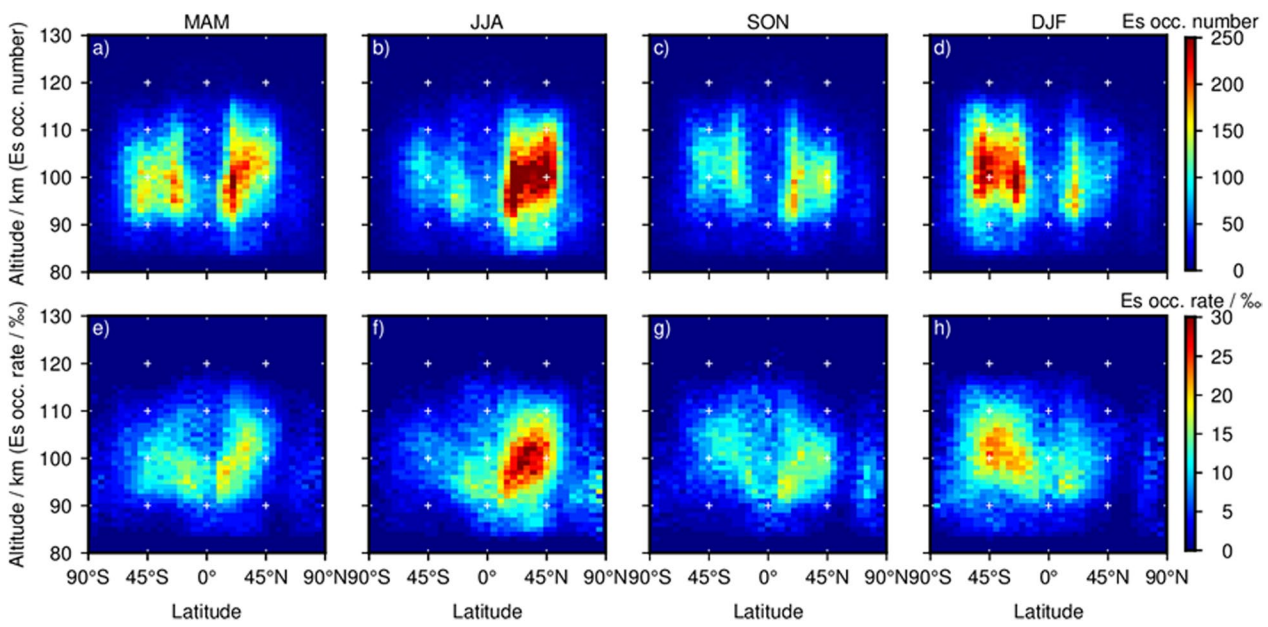

Fig. 11 Seasonal variation in the altitude–latitude distributions of COSMIC RO-derived Es occurrence numbers (upper panels) and occurrence rates (lower panels) during Jan. 2015 to Dec. 2019

variation range and the seasonal distribution patterns of the Es ORs derived based on the data from the two different RO missions independently are basically consistent, while detailed inspections reveal that some differences exist. Firstly, the Es occurrence numbers detected by COSMIC are generally higher than those detected by FY-3C at different altitudes, which is mainly attributed to that the number of the COSMIC RO observations during the studied time period is higher than that of the FY-3C RO ones. Secondly, at the altitudes higher than 105 km, the Es ORs derived by FY-3C data are slightly smaller than those derived by COSMIC data, which is due to that the top heights of the 50-Hz SNR profiles provided by FY-3C are generally lower than those provided by COSMIC. The percentage of the FY-3C profiles reaching 105 km is 77.9%, while for COSMIC, this value is 97.5%. In the present work, to improve the data utilization ratio of FY-3C RO data, all the SNR profiles reaching the height of 80 km are processed for the detection of Es layer, and the Es layers occurring above the top heights of some profiles will not be detected. Thirdly, in the latitude–longitude distributions of the Es ORs, the magnitudes of the FY-3C RO-derived Es occurrences are also generally a little lower than the COSMIC RO-derived ones, which is due to that the Es OR in each $5^\circ \times 5^\circ$ grid is obtained by adding up the numbers of each altitude level, and the deficiency of the Es detections above 105 km leads to the smaller values of the total Es ORs derived by FY-3C RO data.

Figure 12a and b presents the zonal distributions of the Es ORs in the four different seasons during 2015 to 2019 derived from the FY-3C RO data and from the COSMIC RO data, respectively. Here the magnetic latitudes (MLats) are transferred from the geographic latitudes using the International Geomagnetic Reference Field (IGRF)-13 model. Both of the two subfigures show that the seasonal dependency of the zonal distributions of the Es ORs is more distinct in the middle MLat regions than in the low MLat regions. For each season, although the patterns of the variations of the Es ORs with the MLat derived from the two different RO missions are basically consistent with each other, the slightly higher Es ORs derived by COSMIC over different MLat regions can be figured out, and the difference in the magnitudes of the Es ORs derived from the two RO missions becomes apparent in the polar regions. For all the four seasons, at magnetic latitudes higher than 75°N/S, the FY-3C RO-derived Es ORs are close to 0%, while COSMIC RO-derived Es ORs are generally higher than the FY-3C RO-derived ones, reaching around 5 to 10%. Theoretically, the near-polar sun-synchronous orbit of the FY-3C satellite should make it beneficial for probing the ionosphere of the polar regions. In practice, Fig. 2 presents that the volume of the original FY-3C RO observations in the polar regions is non-neglectable, and inspections of the two datasets reveal that at latitudes higher than 75°N/S, the total number of the original RO observations from the FY-3C mission, 64,601, is even higher than that from the COSMIC mission, 62,633. So the distinctly lower FY-3C RO-derived Es ORs should not be attributed to the limited size of the original RO observations. Further inspections of the datasets reveal that during 2015 and 2019, at latitudes higher than 75°N/S, although 96.3% of the original FY-3C RO observations reach the height of 80 km, the ratio of the FY-3C RO observations which reach the height of 90 km is only 25.6%. In comparison, 72% of the original COSMIC RO observations in the polar regions reach the height of 90 km. Due to that most Es layers occur at the altitude higher than 90 km, as shown in Fig. 6 and Fig. 11, the extremely low Es ORs derived from the FY-3C RO mission in polar regions are mainly attributed to the low ratio of the FY-3C RO observations reaching the height of 90 km.

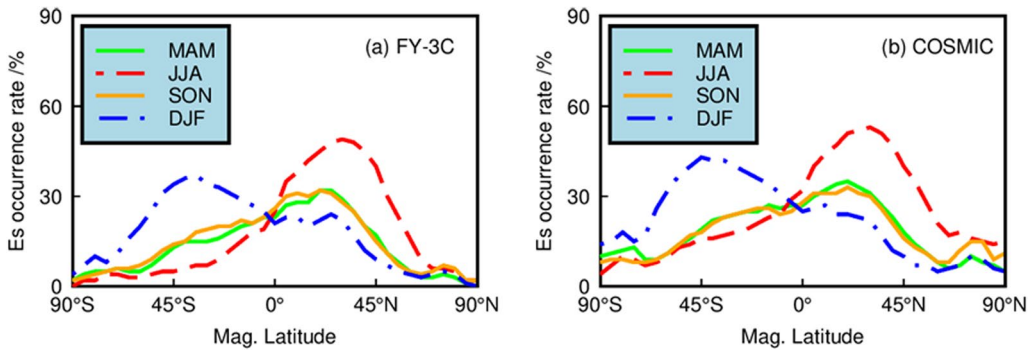

Fig. 12 The zonal distribution of the Es occurrence rates derived from **a** FY-3C RO data and **b** COSMIC RO data in the four different seasons during Jan 2015 to Dec 2019

It should be pointed out that the maximum Es OR derived in the present study using the L1 SNR data from FY-3C RO observations, being around 60%, is basically in accordance with that derived by Arras and Wickert (2018) using the L1 SNR data of COSMIC mission, while is significantly different from some other previous studies. The maximum Es OR during JJA presented by Chu et al. (2014) is only around 10%, which is calculated using the 1-Hz SNR and phase data of the COSMIC RO mission. In Liu et al. (2018), the distributions of Es occurrences are derived using the 50-Hz L1 SNR data of combined RO observations from COSMIC, GRACE and CHAMP, and the maximum value of the occurrence rate during JJA is around 30%. Even with the same type of COSMIC RO data, different schemes applied in data processing will have impacts on the maximum value of the Es OR derived. Qiu et al. (2019) and Luo et al. (2021) both derived the Es ORs using the S4max data from COSMIC mission, while using different data processing strategies, and the maximum Es OR values during summer months obtained by them are around 60% and around 100%, respectively. Like Arras and Wickert (2018), Tsai et al. (2018) derived the Es occurrence using the 50-Hz SNR data of COSMIC RO data, while the maximum Es OR during summer months obtained by them reach around 80%. The comparison between Arras and Wickert (2018) and Tsai et al. (2018) demonstrates that although the threshold for the normalized SNR standard deviation in the Es-layer detection algorithm is set as 0.2 in both of these studies, the width of the sliding window for calculating the standard deviations is different. Moreover, in Arras and Wickert (2018), it is required that large STD values are concentrated within an altitude range of less than 10 km, which means that the irregular amplitude structures with thickness larger than 10 km will not be regarded as Es layers, while in Tsai et al. (2018), about 7% events detected having an Es-layer thickness larger than 10 km.

Due to the different sampling rates of the RO data and the different schemes applied in the data processing, the height range and the thickness ranges of the Es layers detected in different studies are not the same, which leads to that the magnitudes of the Es occurrences derived in these previous studies vary greatly, while the spatial and temporal distribution patterns of the Es-layer occurrences are generally in accordance with each other. The NSMC does not provide S4 index data of FY-3C RO mission, and compared with the 1-Hz RO data, the higher vertical resolution of the 50-Hz RO data is beneficial for observing the Es layers with the thickness of less than 3 km (Tsai et al. 2018). Moreover, considering that the quality of L2 signals degrades much compared with L1 signals, the SNR profiles at L1 band are used here for the detection of Es layers. The Es detection algorithm adopted in the present study is basically consistent with that used by Arras and Wickert (2018), which is the reason why the maximum Es OR derived is also basically in accordance with this reference.

Conclusions

In the present study, the Es layers are detected using the 50-Hz GPS L1 SNR data from the FY-3C RO mission during 2015 to 2019, and the Es-layer morphology derived accordingly is presented. The seasonal variation pattern in the distributions of the FY-3C RO-derived Es ORs is for the first time analyzed and compared with those derived from the COSMIC RO mission. It is found that the seasonal distribution patterns of the FY-3C RO-derived Es ORs, which clearly show the effects of wind shear mechanism and the Earth's magnetic field on the formation of Es layers, are basically consistent with the COSMIC RO-derived ones obtained in other previous studies and in the present work. While further detailed comparison between the Es morphologies obtained by the two RO missions reveals that at the altitudes higher than 105 km, the Es ORs derived by FY-3C data are slightly smaller than those derived by COSMIC data, which is mainly due to that the top heights of the 50-Hz SNR profiles provided by FY-3C are generally lower than those provided by COSMIC. The deficiency of the Es detections above 105 km also leads to the slightly smaller values of the total Es ORs derived by FY-3C RO data in the $5^\circ \times 5^\circ$ grids over the middle and low latitudes. In the polar regions with magnetic latitudes higher than 75°N/S, the COSMIC RO-derived Es ORs are significantly higher than the FY-3C RO-derived ones, which is attributed to the distinctly lower ratio of the FY-3C RO observations reaching the height of 90 km compared with the COSMIC RO ones in these regions. Moreover, due to the near-polar sun-synchronous orbit of the satellite, the spatial coverage of the FY-3C GPS RO data variates in different 1-h local time intervals. During the two local time periods with considerable RO observations over the whole globe, the FY-3C RO-derived Es ORs are generally higher in 9:00–11:00 LT than in 21:00–23:00 LT. The present work reveals that the 50-Hz GPS RO data provided by the GNOS payload aboard the FY-3C satellite can contribute to the study of Es layers, while techniques which help increasing the heights of the upper bounds of these observations are needed for the detections of the complete and detailed structures of Es layers, which is most important for the polar regions. It can be expected that the launch of the following FY-3 series satellites, including FY-E, F, G and R, which will be equipped with the enhanced GNOS payloads, will make more substantial contribution to the ionosphere studies and space weather forecasting.

Abbreviations

CHAMP: Challenging Minisatellite Payload; COSMIC: Constellation Observing System for the Meteorology, Ionosphere, and Climate; DJF: December, January, February; Es: Sporadic E; GPS: Global Positioning System; IGRF: International Geomagnetic Reference Field; JJA: June, July, August; LT: Local time; MAM: March, April, May; NH: Northern hemisphere; ORs: Occurrences rates; RO: Radio occultation; SAA: Southern Atlantic Anomaly; SH: Southern hemisphere; SNR: Signal-to-noise ratio; SON: September, October, November.

Acknowledgements

The authors would like to express their gratitude to the National Satellite Meteorological Centre (NSMC) of China and the University Corporation for Atmospheric Research (UCAR) for providing the Fengyun-3C RO data and the COSMIC RO data, respectively. We are also grateful to the developers of IGRF13 geomagnetic field model (http://www.geomag.bgs.ac.uk/research/modelling/IGRF.html). We thank the two anonymous reviewers for their helpful comments and suggestions.

Author contributions

All authors contributed to the study conception and design. Material preparation and data collection were performed by JL. Data analysis was performed by XX, JL and HW. The draft of the manuscript was written by XX. XX, JL, HL and TH reviewed and completed the manuscript. JL and XX provided project funding supports to this work. All authors read and approved the final manuscript.

Funding

This work is supported by the National Natural Science Foundation of China (Grant Nos. 42074027, 42174017, 41774033 and 41774032).

Availability of data and materials

The data used in the manuscript are all public data. Fengyu-3C RO data can be downloaded from the NSMC: http://satellite.nsmc.org.cn. COSMIC RO data can be downloaded from the CDAAC: https://cdaac-www.cosmic.ucar.edu/cdaac/products.html. The data of geomagnetic field are calculated by IGRF13 geomagnetic field model (http://www.geomag.bgs.ac.uk/research/modelling/IGRF.html).

Declarations

Competing interests

The authors declare no conflict of interests.

Author details

[1]School of Geodesy and Geomatics, Wuhan University, 129 Luoyu Road, Wuhan 430079, China. [2]Collaborative Innovation Center for Geospatial Technology, 129 Luoyu Road, Wuhan 430079, China. [3]Key Laboratory of Geospace Environment and Geodesy, Ministry of Education, 129 Luoyu Road, Wuhan 430079, China.

Received: 22 December 2021 Accepted: 1 April 2022
Published online: 20 April 2022

References

Arras C, Wickert J (2018) Estimation of ionospheric sporadic E intensities from GPS radio occultation measurements. J Atmos Sol Terr Phys 171:60–63. https://doi.org/10.1016/j.jastp.2017.08.006

Arras C, Wickert J, Beyerle G, Heise S, Schmidt T, Jacobi C (2008) A global climatology of ionospheric irregularities derived from GPS radio occultation. Geophys Res Lett. https://doi.org/10.1029/2008GL034158

Bai W, Sun Y, Xia J, Tan G, Cheng C, Yang G, Wang D (2019) Validation results of maximum S4 index in F-layer derived from GNOS on FY3C satellite. GPS Solut 23(1):1–14. https://doi.org/10.1007/s10291-018-0807-x

Chang LC, Chiu PY, Salinas CCJH, Chen SP, Duann Y, Liu JY, Lin CH, Sun YY (2018) On the Relationship Between E Region Scintillation and ENSO Observed by FORMOSAT-3/COSMIC. J Geophys Res Space Phys 123(5):4053–4065. https://doi.org/10.1029/2018JA025299

Chu YH, Wang CY, Wu KH, Chen KT, Tzeng KJ, Su CL, Feng W, Plane JMC (2014) Morphology of sporadic E layer retrieved from COSMIC GPS radio occultation measurements: wind shear theory examination. J Geophys Res Space Phys 119(3):2117–2136. https://doi.org/10.1002/2013JA019437

Haldoupis C (2012) Midlatitude sporadic E A typical paradigm of atmosphere–ionosphere coupling. Space Sci Rev 168(1):441–461. https://doi.org/10.1007/s11214-011-9786-8

Haldoupis C, Pancheva D, Mitchell NJ (2004) A study of tidal and planetary wave periodicities present in midlatitude sporadic E layers. J Geophys Res Space Phys. https://doi.org/10.1029/2003JA010253

Hocke K, Igarashi K, Nakamura M, Wilkinson P, Wu J, Pavelyev A, Wickert J (2001) Global sounding of sporadic E layers by the GPS/MET radio occultation experiment. J Atmos Sol Terr Phys 63(18):1973–1980. https://doi.org/10.1016/S1364-6826(01)00063-3

Liao SM, Xu JS, Cheng J (2016) Longitudinal Variations of Es layers irregularities based on GPS-CHAMP occultation measurements (2001–2008). Chinese J Geophys 59(8):2739–2746. https://doi.org/10.6038/cjg20160801 (**in Chinese**)

Liu Y, Zhou C, Tang Q, Li Z, Song Y, Qing H, Ni B, Zhao Z (2018) The seasonal distribution of sporadic E layers observed from radio occultation measurements and its relation with wind shear measured by TIMED/TIDI. Adv Space Res 62(2):426–439. https://doi.org/10.1016/j.asr.2018.04.026

Luo J, Liu H, Xu X (2021) Sporadic E morphology based on COSMIC radio occultation data and its relationship with wind shear theory. Earth Planets Space 73:212. https://doi.org/10.1186/s40623-021-01550-w

Mao T, Sun L, Yang G, Yue X, Yu T, Huang C, Wang J (2016) First ionospheric radio-occultation measurements from GNSS occultation sounder on the Chinese Feng-Yun 3C satellite. IEEE Trans Geosci Remote Sens 54(9):5044–5053. https://doi.org/10.1109/TGRS.2016.2546978

Mathews JD (1998) Sporadic E: current views and recent progress. J Atmos Sol Terr Phys 60(4):413–435. https://doi.org/10.1016/S1364-6826(97)00043-6

Niu J, Weng LB, Meng X, Fang HX (2019) Morphology of ionospheric sporadic e layer intensity based on COSMIC occultation data in the midlatitude and low-latitude regions. J Geophys Res Space Phys 124(6):4796–4808. https://doi.org/10.1029/2019JA026828

Ogawa T, Suzuki A, Kunitake M (1989) Spatial distribution of mid-latitude sporadic E scintillations in summer daytime. Radio Sci 24(04):527–538. https://doi.org/10.1029/RS024i004p00527

Pirscher B, Foelsche U, Lackner BC, Kirchengast G (2007) Local time influence in single-satellite radio occultation climatologies from Sun-synchronous and non-Sun-synchronous satellites. J Geophys Res Atmos. https://doi.org/10.1029/2006JD007934

Qiu L, Zuo X, Yu T, Sun Y, Qi Y (2019) Comparison of global morphologies of vertical ion convergence and sporadic E occurrence rate. Adv Space Res 63(11):3606–3611. https://doi.org/10.1016/j.asr.2019.02.024

Qiu L, Yu T, Yan X, Sun YY, Zuo X, Yang N, Wang J, Qi Y (2021) Altitudinal and latitudinal variations in ionospheric sporadic-E layer obtained from FORMOSAT-3/COSMIC radio occultation. J Geophys Res Space Phys 126:e2021JA029454. https://doi.org/10.1029/2021JA029454

Tsai LC, Su SY, Liu CH, Schuh H, Wickert J, Alizadeh MM (2018) Global morphology of ionospheric sporadic E layer from the FormoSat-3/COSMIC GPS radio occultation experiment. GPS Solut 22(4):118. https://doi.org/10.1007/s10291-018-0782-2

Wang H, Luo J, Xu X (2019) Ionospheric peak parameters retrieved from FY-3C radio occultation: a statistical comparison with measurements from COSMIC RO and digisondes over the globe. Remote Sens 11(12):1419. https://doi.org/10.3390/rs11121419

Whitehead JD (1961) The formation of the sporadic-E layer in the temperate zones. J Atmos Terr Phys 20(1):49–58. https://doi.org/10.1016/0021-9169(61)90097-6

Whitehead JD (1970) Production and prediction of sporadic E. Rev Geophys 8(1):65–144. https://doi.org/10.1029/RG008i001p00065

Whitehead JD (1989) Recent work on mid-latitude and equatorial sporadic E. J Atmos Terr Phys 51(5):401–424. https://doi.org/10.1016/0021-9169(89)90122-0

Wu DL, Ao CO, Hajj GA, de La Torre JM, Mannucci AJ (2005) Sporadic E morphology from GPS-CHAMP radio occultation. J Geophys Res Space Phys. https://doi.org/10.1029/2004JA010701

Xue Z, Yuan Z, Liu K, Yu X (2018) Statistical research of Es distribution in inland areas of China based on COSMIC occultation observations. Chinese J Geophys 61(8):3124–3133. https://doi.org/10.6038/cjg2018L0670 (**in Chinese**)
Yang J, Huang J, Jie X, Deng B, Quan H (2016) Study of Sporadic E layers based on occultation data observed by FY-3C satellite. Chin J Space Sci 36(3):305–311. https://doi.org/10.11728/cjss2016.03.305 (**in Chinese**)
Yeh WH, Huang CY, Hsiao TY, Chiu TC, Lin CH, Liou YA (2012) Amplitude morphology of GPS radio occultation data for sporadic-E layers. J Geophys Res Space Phys. https://doi.org/10.1029/2012JA017875
Yu B, Xue X, Yue XA, Yang C, Yu C, Dou X, Ning B, Hu L (2019) The global climatology of the intensity of the ionospheric sporadic E layer. Atmos Chem Phys 19(6):4139–4151. https://doi.org/10.5194/acp-19-4139-2019
Yue X, Schreiner WS, Zeng Z, Kuo YH, Xue X (2015) Case study on complex sporadic E layers observed by GPS radio occultations. Atmos Meas Tech 8(1):225–236. https://doi.org/10.5194/amt-8-225-2015
Zeng Z, Sokolovskiy S (2010) Effect of sporadic E clouds on GPS radio occultation signals. Geophys Res Lett. https://doi.org/10.1029/2010GL044561
Zhou C, Tang Q, Song X, Qing H, Liu Y, Wang X, Gu X, Ni B, Zhao Z (2017) A statistical analysis of sporadic E layer occurrence in the midlatitude China region. J Geophys Res Space Physics 122:3617–3631. https://doi.org/10.1002/2016JA023135

Publisher's Note